P2.42 VISIBLE CLEAR-SKY AND NEAR-INFRARED SURFACE ALBEDOS DERIVED FROM VIRS DATA FOR CERES

Sunny Sun-Mack, Yan Chen, Tim D. Murray
Science Applications International Corporation, Hampton, Virginia

Patrick Minnis*, David F. Young
Atmospheric Sciences, NASA Langley Research Center, Hampton, VA

1. INTRODUCTION

One of the critical parameters for detecting clouds and for deriving their microphysical properties is the clear-sky radiance. Knowledge of the spatial and angular variability of clear-sky albedo is an essential first step for predicting the clear-sky radiance at solar wavelengths. Two spectra used in the detection and classification of clouds for the Clouds and the Earth's Radiant Energy System (CERES) Experiment are the visible (VIS; 0.65 μm) and near-infrared (NIR; 1.6 μm) channels on the imagers used by CERES. The first imager used by CERES is the Visible Infrared Scanner (VIRS) on the Tropical Rainfall Measuring Mission (TRMM) satellite. Because of TRMM's 35°-inclined-orbit, the VIRS takes measurements at all times of day over a given region between 38°N and 38°S during a period of 46 days. Unlike geostationary satellite measurements which are all taken from a fixed viewing zenith angle, the precessing VIRS can observe a given scene from a variety of angles over a period of time, thus minimizing the impact of bidirectional reflectance distribution functions (BRDF) errors in the determination of monthly mean albedo. Instantaneous albedos, however, remain subject to all of the uncertainties in the BRDFs.

The 2-km VIRS imagery also provides the first opportunity for deriving the 1.6-μm albedo and its solar zenith angle SZA dependence for much of the Earth's surface and all of its major surface types. This paper describes the initial results from an analysis of VIRS clear radiances (as identified by CERES) to derive the VIS clear-sky and NIR surface albedos at a 10' resolution between 38°N and 38°S during January 1998.

*Corresponding author address: Patrick Minnis, NASA Langley Research Center, MS 420, Hampton, VA 23681-2199. email: p.minnis@larc.nasa.gov.

2. METHODOLOGY

The observed clear-sky reflectance is

$$\rho_\lambda = \rho_\lambda(K; LAT, LON; \mu_o, \mu, \psi) \quad (1)$$

where λ is the wavelength, K is the International Geosphere Biosphere Programme (IGBP) surface type (see Table 1), LAT and LON are the latitude and longitude, respectively, μ_o and μ are the cosines of the solar and viewing zenith angles, respectively, and ψ is the relative azimuth angle. The clear-sky reflectance is a combination of radiation reflected by the atmosphere and by the surface. For the VIS channel, the primary atmospheric effects are Rayleigh and aerosol scattering and ozone absorption, while water vapor absorption and aerosols are the primary attenuators in the near-infrared channel.

2.1 NIR surface albedos

Neglecting aerosols, the observed NIR reflectance can be approximated as,

$$\rho_{NIR} = \alpha_{sNIR}\, \chi_{NIR}\, (K; \mu_o, \mu, \psi)\, t_{NIR}, \quad (2)$$

Where α_{sNIR} is the surface albedo and χ_{NIR} is the normalized BRDF for the surface, and t_{NIR} is the combined transmittance of the atmosphere to the downwelling solar beam and upwelling diffuse radiation. It is estimated as

$$t_{NIR} = \exp[-\tau_{NIR}(1/\mu_o + 2.04)], \quad (3)$$

where τ_{NIR} is the water vapor optical parameterized as a function of the precipitable water, surface pressure, μ_o, and LAT based on the results of detailed radiative transfer calculations using correlated k-distribution calculations for the VIRS NIR channel following the method of Kratz (1995).

Table 1. Surface type classification for CERES

K	IGBP type
1	evergreen needleleaf
2	evergreen broadleaf
3	deciduous needleleaf
4	deciduous broadleaf
5	mixed forest (conifer + broadleaf)
6	closed shrublands
7	open shrubland
8	woody savanna
9	savanna
10	grassland
11	permanent wetlands
12	croplands
13	urban
14	mixed grass-forest
15	snow/ice
16	desert, barren/sparse vegetation
17	water
18	tundra
19	coastline (10 to 90% water)

The NIR BRDFs for most of the surface types were derived from the aircraft measurements of Kriebel (1978) taken at 1.66 μm for four distinct surfaces. The coniferous forest model was used for all forest types (K = 1,5), while bog was used for K = 11, 18, and 19. The savanna data were used for K = 6, 7, 8, 9, and 13 and the pasture results were used for K = 10, 12, and 14. The updated VIS model for ocean from Minnis and Harrison (1984) was used for water, while the shortwave snow and desert models from Suttles et al. (1988) were used for K = 15 and 16, respectively.

The mean SZA-dependent albedos $\alpha_{NIR}(K; \mu_o)$ or directional reflectance models (DRM) were derived by initially processing the data to obtain albedos for each clear pixel and then averaging all of the albedos for a given IGBP type into SZA bins defined by 0.1 intervals of μ_o. Because of sparse sampling, noise, and similarities in α_{NIR} for some surface types, many of the results were averaged to obtain means for a set of IGBP types. Normalized DRMs are then

$$\delta_{NIR}(K;\mu_o) = \alpha_{NIR}(K; \mu_o) / \alpha_{NIR}(K; \mu_o=0.95). \quad (4)$$

The results were fitted to a third-order polynomial to obtain a smooth curve for each surface type.

After creating the normalized DRMs, the data were reanalyzed on a 10' grid. Whenever a clear reflectance was observed for a given 10' box, the surface albedo at $\mu_o = 1$ was computed using (2) and (4) and summed into a running mean for the month. In this manner, a monthly mean, overhead-sun NIR surface albedo was computed for each region. These results were averaged to obtain a mean albedo for each IGBP type. All regions lacking an observed average were then filled with the IGBP mean overhead-sun albedo.

2.2 VIS clear-sky albedos

Similarly, the top-of-the-atmosphere VIS albedo is

$$\alpha_{VIS} = \rho_{VIS}(K; LAT,LON;\mu_o,\mu,\psi) / \chi_{VIS}(K; \mu_o,\mu,\psi), \quad (5)$$

where the VIS BRDFs are taken from Minnis and Harrison (1984) for water and from Suttles et al. (1988) for land (K = 1-14, 18), snow, and desert. The observed reflectances were converted to TOA albedo and binned according to SZA in the same manner as the NIR data. After combining regions with similar results, normalized VIS DRMs were generated using least squares regression fits to third-order polynomials from the normalized albedos,

$$\delta_{VIS}(K;\mu_o) = \alpha_{VIS}(K; \mu_o) / \alpha_{VIS}(K; \mu_o=0.95). \quad (6)$$

The VIS DRMs were forced to a value of unity at overhead sun. Regional overhead-sun albedos were then generated on a 10' grid from clear-sky data in the same fashion as the NIR albedos.

3. DATA

The TRMM orbit allows the VIRS to sample all local hours of a given region near the Equator over a period of 23 days compared to 46 days at the orbit inclination latitude. Thus, for much of the potential viewing area, the full range of possible SZAs could be sampled in a given region. Due to cloud cover, however, the number of samples in a given 10' box is reduced substantially except over desert areas. Data used to compute the regional albedos were selected in the following manner. First, the CERES cloud mask (Trepte et al., 1999) was used to classify pixels as clear or cloudy. This cloud mask uses a variety of thresholds determined from the estimates of the clear-sky VIS albedo and brightness temperatures at 3.7, 10.8, and 12 μm. The initial clear-sky albedos for establishing the reflectance thresholds were derived from International Satellite

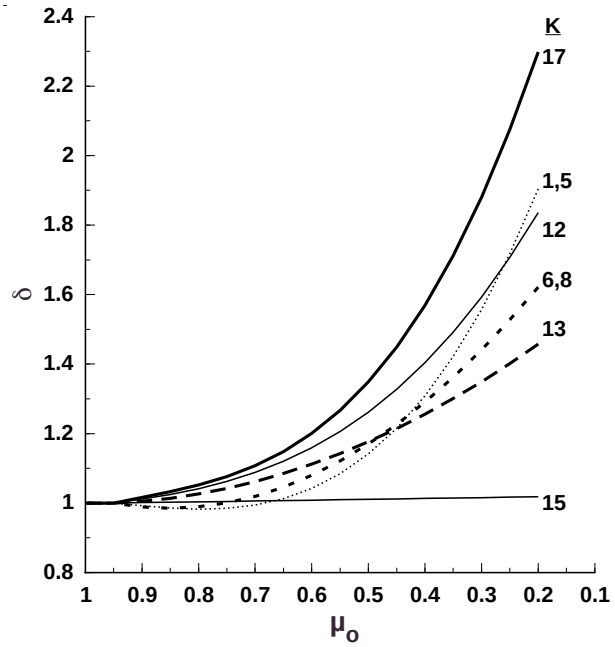

Fig. 1. Visible DRMs from VIRS, January 1998.

Cloud Climatology Project (ISCCP; see Schiffer and Rossow, 1985) Advanced Very High Resolution Radiometer DX clear-sky reflectances for January 1986. The reflectances were converted to overhead-sun albedos using the Suttles et al. (1988) BRDFs and DRMs and multiplied by 0.85 to account for calibration differences. Clear-sky reflectance for water was estimated with the Minnis and Harrison (1984) models. The NIR atmospheric optical depths were computed using the soundings from the CERES Model Ozone and Atmosphere profiles of temperature and humidity. Because of a flaw in the VIRS NIR filter, thermal infrared radiation contaminated the radiance. A correction was applied to remove the contaminating radiance.

After a pixel was classified as clear, it was used in the computation of a mean overhead-sun clear-sky (VIS) or surface (NIR) albedo for its particular 10' region. Only data for SZA $\leq$ 78° were used.

4. RESULTS

VIS DRMs were derived for all surfaces except for snow, desert, and K= 3. The desert data were not used to develop a VIS DRM because of the large range in desert albedo compared to other surface types. The data were biased by preferential sampling of particular locations with μ_o. Insufficient samples were obtained for the other two surfaces. All of the forest types were combined into one model, while one DRM was derived for combinations of K = 6 and 8 and K = 9 and 10.

Table 2. Overhead-sun albedos from VIRS

K	α_{VIS}	α_{NIR}
1	0.105	0.169
2	0.097	0.169
3	0.093	0.169
4	0.088	0.169
5	0.086	0.169
6	0.115	0.223
7	0.161	0.325
8	0.100	0.225
9	0.130	0.269
10	0.135	0.269
11	0.099	0.204
12	0.111	0.249
13	0.121	0.221
14	0.094	0.205
15	0.187	0.235
16	0.594*	0.177*
17	0.057	0.021
18	0.162	0.206
19	0.090	0.132

*μ_o = 0.55

Examples of the derived normalized DRMs are shown in Fig. 1. Mean overhead albedos are shown in Table 2 for both channels. Typically, the darkest surfaces show the greatest rise in δ with decreasing μ_o. DRMs for the other surface types are close to one of those shown in Fig. 1. The ERBE desert model is similar to that for K = 13. Mean desert VIS albedos range from ~0.15 to more than 0.50 over parts of the Sahara, thus the mean albedo for K = 16 is not particularly representative for most deserts. Few of the VIS models have values less than unity over all μ_o's. These variations of $\delta_{VIS}(\mu_o)$ are similar to those for broadband shortwave radiation, but are much different from those seen for $\delta_{NIR}(\mu_o)$.

Figure 2 shows $\delta_{NIR}(\mu_o)$ for relatively distinct models. The water model is similar to the VIS model except for the dip below unity in the middle angles. The lower albedo forest models show a monotonic increase with μ_o, while absorption becomes more significant as the SZA increases for the higher albedo surfaces. This behavior is similar to that observed by Kriebel (1978) for the 1.66-μm data.

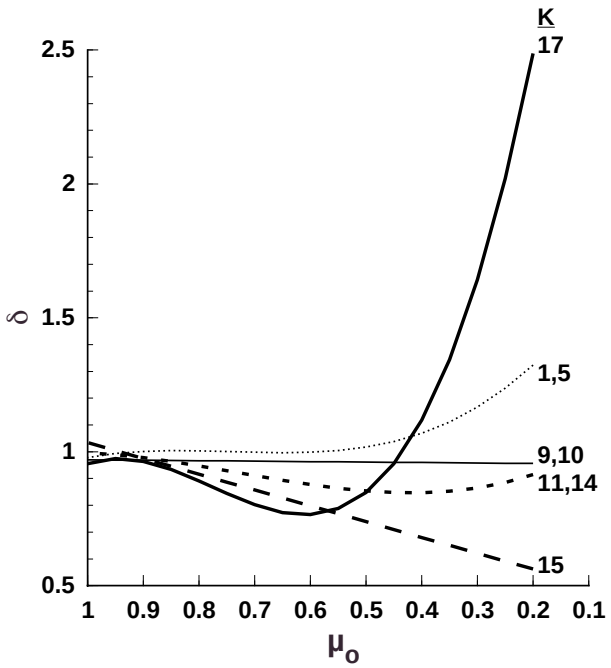

Fig. 2. Same as Fig. 1, except for 1.6 μm.

The snow data are sparsely sampled, so it is not clear if the decrease in δ with μ_o is significant.

Except for snow and water, the NIR albedos are much greater than their VIS counterparts. The NIR desert albedos range from 0.20 to more than 0.70 over parts of the Sahara. At overhead sun, the ratio of VIS-to-NIR albedo varies from roughly 1.6 to 2.3 for most vegetated land surfaces. Dry surfaces like tundra and desert have values around 1.3, while ice and water have ratios smaller than 0.5. These ratios vary with SZA also. Figure 3 shows selected mean reflectance ratios observed at various SZAs. Except for deserts, the ratios tend to decrease with decreasing μ_o. Despite the geographical variability of the desert albedos, the desert ratios are relatively constant between 1.3 and 1.5. Thus, ρ_{NIR} for a given area may be predicted relatively accurately given a value of ρ_{VIS}. The observed means for the albedos and the reflectance ratios have standard deviations of ~30% for most SZA bins. The variance in the values arises from BRDF uncertainties, local changes in soil moisture and vegetation, and variability within a given scene type.

5. CONCLUDING REMARKS

These preliminary results represent the first assessment of the SZA-dependence of VIS and NIR albedos on a near-global scale. Some surface types can be grouped together to develop SZA-dependent albedo models. Further analyses will use new BRDF models and VIRS data from other months to improve the statistics. The availability of this database for both VIS and NIR albedos should greatly enhance the automatic classification of scenes in satellite remote sensing.

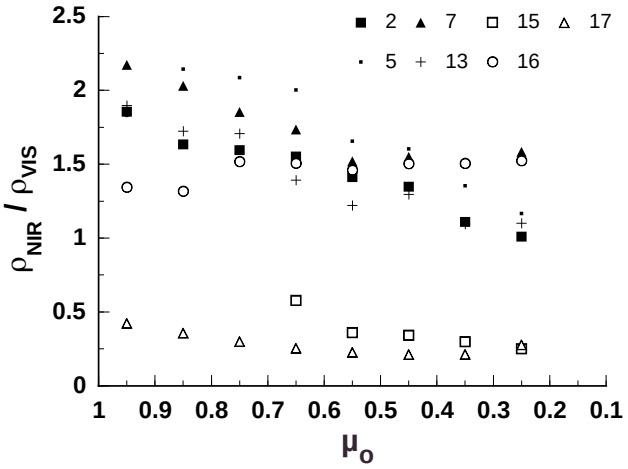

Fig. 3. Mean 1.6/0.65-μm clear-sky reflectance ratios.

6. References

Kratz, D. P., 1995: The correlated k-distribution technique as applied to the AVHRR channels. J. Quant. Spectrosc. Radiat. Transfer, **53**, 501-507.

Kriebel, K. T., 1978: Measured spectral bidirectional reflectance properties of vegetated surfaces. Appl. Opt., **17**, 253-259.

Minnis, P. and E. F. Harrison, 1984: Diurnal variability of regional cloud and clear-sky radiative parameters derived from GOES data. Part III: November 1978 radiative parameters. J. Climate Appl. Meteor., **23**, 1032-1051.

Schiffer, R. A., and W. B. Rossow, 1985: ISCCP global radiance data set: A new resource for climate research. Bull. Amer. Meteor. Soc., **66**, 1498-1505

Suttles, J. T., R. N. Green, P. Minnis, G. L. Smith, W. F. Staylor, B. A. Wielicki, I. Walker, D. F. Young, V. R. Taylor, and L. L. Stowe, 1988: Angular radiation models for Earth-atmosphere system, Vol. 1, Shortwave radiation. NASA RP-1184, 144 pp.

Trepte, Q., Y. Chen, S. Sun-Mack, P. Minnis, D. F. Young, B. A. Baum, P. W. Heck, 1999: Scene identification for the CERES cloud analysis subsystem. Proc. AMS10th Conf. Atmos. Rad., 28 June – 2 July, Madison, WI.